ADVANCED FUNCTIONAL MATERIALS
www.afm-journal.de

www.MaterialsViews.com

Rational Design of Small Molecules to Implement Organic Quaternary Memory Devices

Qijian Zhang, Jinghui He, Hao Zhuang, Hua Li, Najun Li, Qingfeng Xu, Dongyun Chen, and Jianmei Lu**

Organic small-molecule-based devices with multilevel electroresistive memory behaviors have attracted more and more attentions due to their super-high data-storage density. However, up to now, only ternary memory molecules have been reported, and ternary storage devices may not be compatible with the binary computing systems perfectly. In this work, a donor–acceptor structured molecule containing three electron acceptors is rationally designed and the field-induced charge-transfer processes can occur from the donors. Organic quaternary memory devices based on this molecule are successfully demonstrated for the first time. The switching threshold voltages of the memory device are –2.04, –2.73, and –3.96 V, and the current ratio of the "0," "1," "2," and "3" states is $1:10^{1.78}:10^{3.47}:10^{5.36}$, which indicate a low possibility of read and write errors. The results represent a further step in organic high-density data-storage devices and will inspire the further study in this field.

1. Introduction

Since conventional memories have almost been reaching their downscaling limits and cannot meet the ever-growing demand of information explosion, resistance switching random access memory (RRAM) gradually attracted both fundamental and industrial interests.[1–4] The memory behaviors in RRAMs depend on different resistance/conductance states under an external electric field, namely high-resistance/low-conductance (OFF) state or low-resistance/high-conductance (ON) state. Furthermore, RRAM appears to be a candidate of new generation memory due to its simple structure, stacking feasibility, long retention time, and low power consumption.[5–11] In addition, being a simple metal/active material/metal sandwiched structure, RRAM is facile to be stacked layer by layer, which is able to increase the information density dramatically.[12,13] Intensive research has revealed that many inorganic oxides,[14] polymers,[15] and small molecules[16–18] demonstrate resistive switching memory behaviors. Among them, small molecules have recently attracted more and more attentions because of their tunable structures, easy purification, flexibility, and low cost.[16–18] Particularly, typical donor–acceptor (D–A) conjugated molecules have been proved to be one of the most successful active materials in the design of memory devices since the charge-transfer (CT) process can occur when an external electric field is applied, resulting in the abrupt conductivity switching.[19]

Currently, the memory devices we utilized are mainly binary memory systems, and it is difficult to further increase the storage capacity owing to the limitations of physical factors or process technology.[20–22] However, an increase in the number of conductive states (i.e., 0, 1, 2, and 3) in memory device can improve the data-storage capacity exponentially.[19a] Thus, much attention has been paid to seeking novel materials with multilevel memory effects. After years of exploration, organic ternary resistive memory device was first realized in our group through introducing two different electron-deficient moieties in a small molecule to forming two various charge-trapping sites.[23] Indeed, the storage density is improved from 2^n to 3^n, which is a great breakthrough in memory devices. Subsequently, Huang et al. designed a ternary memory device by combining charge-transfer and conformational change switching mechanisms into a single polymer.[24] Recently, Yam et al. reported a small-molecule-based high-performance ternary memory device induced by two charge-transfer processes.[19a] However, the conductive switching mechanism is still ambiguous in organic materials, which hindered the further understanding and rational design of new organic molecules with multilevel memory behaviors. Additionally, although ternary memory devices increase the storage capacity largely, they may have difficulty in coupling with the present binary computing systems. To better match current microelectronic techniques and simultaneously meet super-high memory capacity, quaternary logic storage is coming into sight, which can further increase the storage capacity to amazing 4^n and can easily match the present binary system as it can be decoded directly into two binary-digit equivalents.[25–27] However, quaternary RRAMs have only been

Dr. Q. Zhang, Prof. J. He, Dr. H. Zhuang,
Prof. H. Li, Prof. N. Li, Prof. Q. Xu,
Prof. D. Chen, Prof. J. Lu
College of Chemistry
Chemical Engineering and Materials Science
Collaborative Innovation Center of Suzhou
Nano Science and Technology
Soochow University
Suzhou 215123, P. R. China
E-mail: lihuaw@suda.edu.cn; lujm@suda.edu.cn

DOI: 10.1002/adfm.201503493

achieved for inorganic and hybrid materials,[28–31] and there is no report about organic quaternary RRAM device up to now.

In this work, based on the charge-transfer mechanism, D–A conjugated molecules containing distinct electron acceptors may produce multilevel memory behaviors.[19] This inspires us to design small molecules containing three different electron acceptors, hopefully of quaternary memory behaviors. Structurally, it is reported that symmetric conjugated molecules are beneficial for the crystallinity in film state and, in consequence, the working parameters of the memory devices.[17c,18d] Therefore, three types of acceptors symmetrically distributed on each side of a molecular backbone are expected to produce better memory performance. However, this will cause the number of required acceptors to double and the target molecule will be of poor solubility and thus challenging to synthesize. Thus, we trade off the molecular symmetry and part of planarity to consider designing an asymmetric molecule containing three different electron-withdrawing units together with donors and conjugated backbones; organic quaternary memory devices were successfully fabricated for the first time with distinct current ratios and identified threshold voltages of the four conductive states.

2. Results and Discussion

2.1. Synthesis and Characterization

First, we select three electron acceptors from those who demonstrate promising performance in photovoltaic devices.[19,32–35] Benzo[c][1,2,5]thiadiazole (BTD) has been recognized as one of the most attractive moieties in the design of photoelectric materials due to its relatively weak electron-accepting capability.[19,32] 1,8-Naphthalimide (NI) unit and nitro (NO) group are attractive electron acceptors and have good thermal stability, chemical inertness, and excellent processability.[34] Meanwhile, thiophene (T) as the donor is chosen to promote the molecular planarity and the hole-transporting property.[33,36] The formed D–A structured dithienyl substituted benzothiadiazole (BTDT) core may result in the intramolecular hydrogen bonds between the nitrogen atom of the BT unit and the active hydrogen atom of thiophene units, which is also beneficial for the molecular planarity.[37] The conjugated plane is conductive to the CT process and can induce intense π–π stacking interactions thus lowering down the energy barriers.[38] However, the planar conjugated backbone has a tendency to aggregate in common solvents, which will increase the difficulty in synthesizing.[38] Thus, hexyl side chains are introduced into the backbone to increase the solubility and to form the ordered structure via intermolecular interdigitation.[33,39] **Figure 1** shows the structures of our designed asymmetric molecule 6-(5-(7-(5-(9-(2-ethylhexyl)-6-nitrocarbazol-3-yl)-4-hexylthiophen-2-yl)benzo[c][1,2,5]thiadiazol-4-yl)-3-hexylthiophen-2-yl)-2-octyl-1H-benzo[de]isoquinolin-e-1,3(2H)-dione (NONIBTDT) and its symmetric analogs 4,7-bis(5-(9-(2-ethylhexyl)-6-nitro-9H-carbazol-3-yl)-4-hexylthiophen-2-yl)benzo[c][1,2,5]thiadiazole (DNOBTDT) with only two electron acceptors as the control. The detailed synthetic routes and product analysis were summarized in Schemes S1 and S2 in the Supporting Information. Thermogravimetric analysis and differential scanning calorimetry measurements were carried out to measure the thermal properties of both molecules, as shown in Figures S17 and S18 (Supporting Information).

2.2. Theoretical Calculations

Theoretical electrostatic potential (ESP) surface was calculated through density functional theory (DFT) to confirm the various electron-withdrawing capabilities of BTD, NI, and NO acceptors. As shown in Figure 1a, DFT molecular simulation result shows an open channel from the molecular surface throughout the conjugated backbone with continuous positive molecular electrostatic potential (in yellow), indicating that the charge carriers could migrate throughout this open channel with freedom. Additionally, the negative molecular ESP regions (in green) in molecular backbones are attributed to BTD, NI, and NO acceptors for NONIBTDT. These negative regions with various ESP plottings are consistent with the electron-accepting capabilities of electron acceptors. Thus, the electron-deficient capability of NI is stronger than that of BTD, and that of NO is recognized as the strongest. As a control molecule (Figure 1b), DNOBTDT only processes a weakest electron-acceptor BTD and two strongest electron-deficient NO moieties.

2.3. Memory Devices Performance

Subsequently, the electronic properties of NONIBTDT and DNOBTDT-based memory devices were measured to confirm the multilevel memory behaviors. The graph in the inset of

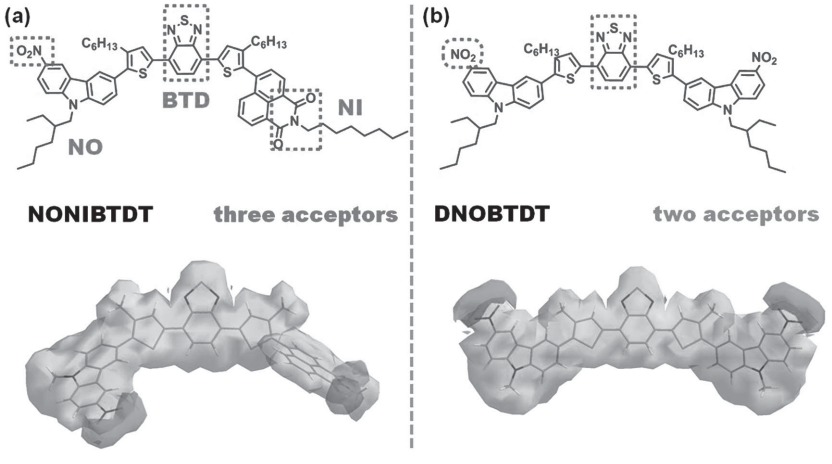

Figure 1. The molecular structure and the result of DFT simulation (top) for the ESP plotting (bottom) of a) NONIBTDT and b) DNOBTDT. Molecule NONIBTDT contains three electron acceptors, NO, NI, and BTD, shown as the green part in the ESP plotting, while DNOBTDT contains two electron-deficient moieties in the backbone.

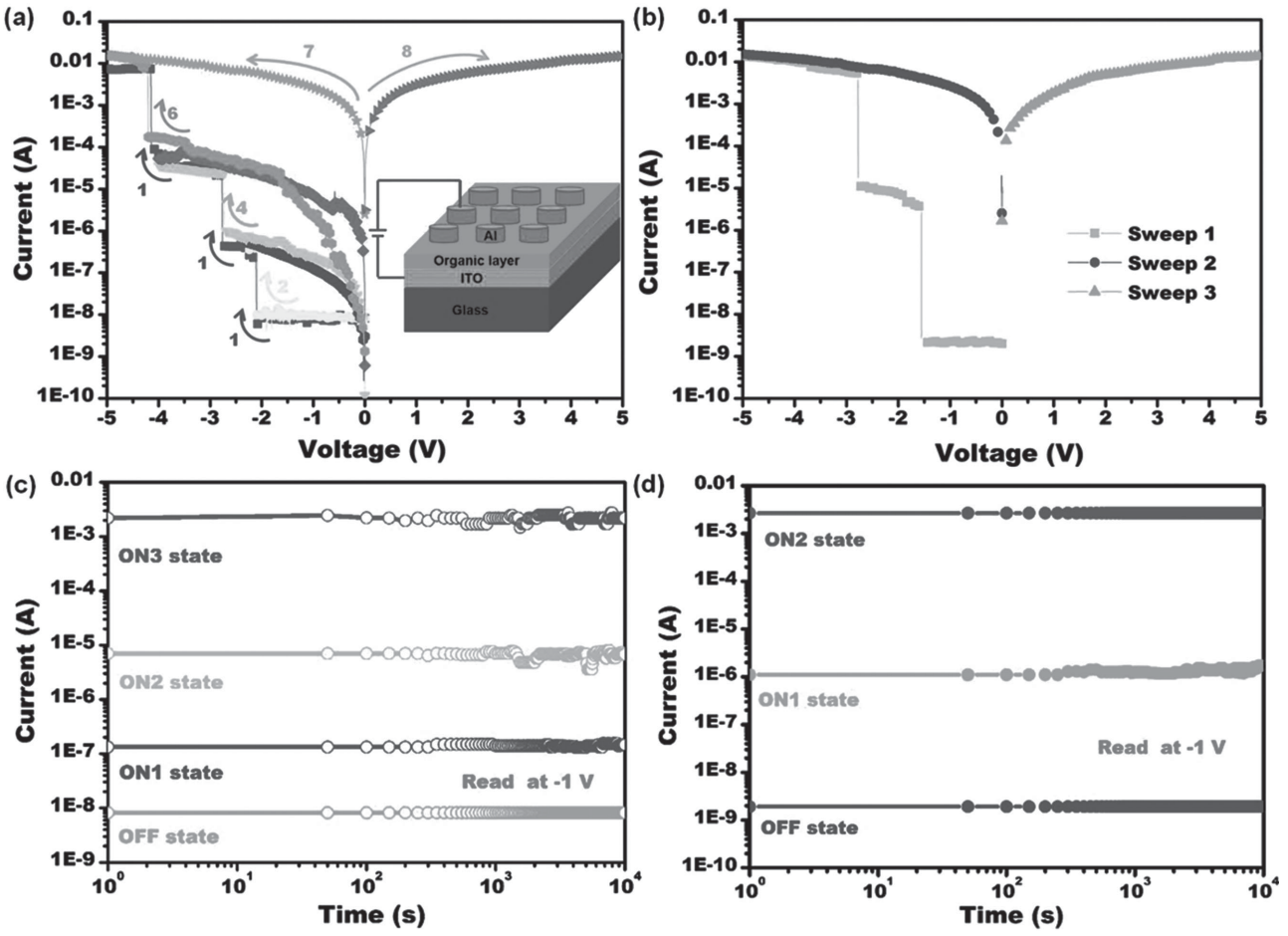

Figure 2. a) The electrical characteristics of NONIBTDT-based memory devices. Sweep 1 shows three sharp jumps of current when the voltage is from 0 to –5 V. Sweeps 2, 4, and 6 are successively performed to exhibit conductive transitions from "OFF" state to the "ON1" state, then to the "ON2" state and finally to the "ON3" state. Sweeps 7 and 8 show the WORM behavior of the memory device. The inset in panel (a) shows the sandwich-structured memory device, consisting of ITO substrate, active layer, and Al electrode. b) The ternary electrical characteristics of DNOBTDT-based memory device. c) Stability tests of NONIBTDT-based device under constant voltage stress at –1 V. d) Stability tests of DNOBTDT-based device under constant voltage at –1 V.

Figure 2a shows the structure of the memory device consisting of a layer of indium tin oxide (ITO) on a glass substrate as the bottom electrode, a spin-coated 90 nm thick organic layer covered by a vacuum-deposited 150 nm thick Al top electrode, as confirmed by the scanning electron microscopy (SEM) image (Figure S1, Supporting Information). The electronic characteristics of NONIBTDT-based memory devices were summarized on about 20 cells. This ITO/NONIBTDT/Al device lies in the low-conductance state ("OFF" state) when a small "reading" voltage (–1 V) is applied. When an external voltage from 0 to –5 V was gradually swept on the device, three abrupt jumps of current were observed at the switching threshold voltages of approximately –2.04, –2.73, and –3.96 V, illustrating three new conductive states of the device, namely "ON1," "ON2," and "ON3," or corresponding to four storage states, "0," "1," "2," and "3." Sweeps 2, 4, and 6 were performed on other fresh cells, indicating that the device can successively transition from the OFF state ("0" state) to the ON1 state ("1" state), then from the ON1 state ("1" state) to the ON2 state ("2" state), and finally from the ON2 state ("2" state) to the ON3 state ("3" state). Once the device reached the ON3 state, neither negative bias nor positive voltage could turn the system back to the initial OFF state (sweeps 7 and 8). Therefore, the NONIBTDT-based device exhibits a quaternary write-once-read-many-times (WORM) memory behavior. Furthermore, the ratio of these conductive states of the "0," "1," "2," and "3" states is $1:10^{1.78}:10^{3.47}:10^{5.36}$, which indicate a low possibility of read and write errors. Further measurements (**Figure 3**c) showed that NONIBTDT-based memory device was stable under a constant voltage of –1 V for 10^4 s without degradation. This indicates that this quaternary device may be of potential applications in practical organic memory devices.

In order to rule out the formation of conduction filaments in the films, an Hg droplet is applied to replace thermally evaporated Al as the top electrode. As we know, Hg is a less reactive metal and is very stable in the atmosphere of oxygen. Furthermore, Hg is not easily penetrating into the organic layer to form metallic filaments in the thin films. As shown in Figure S7 (Supporting Information), the memory device also shows three sharp increases in current that corresponds to the quaternary memory behavior.

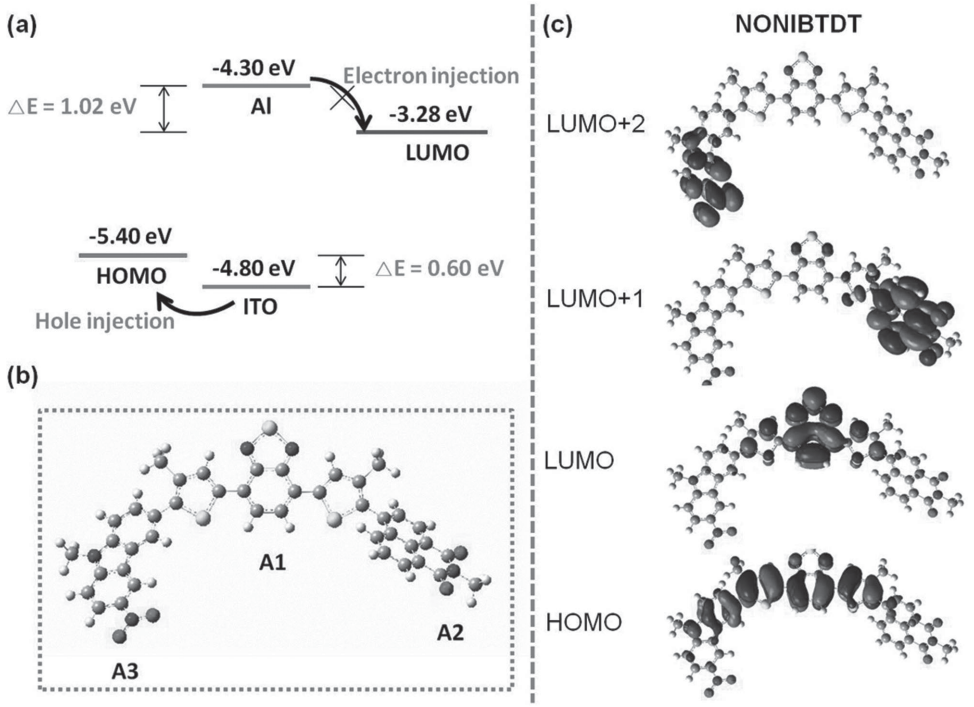

Figure 3. a) Schematic illustration of the charge-transfer process of NONIBTDT-based memory device. b) The optimal structural backbone of molecule NONIBTDT. c) Spatial plots of the molecular orbitals for NONIBTDT.

To further confirm that the memory behavior originates from the inherent property of the molecule itself, an LiF layer of 5 nm thickness was evaporated as a buffer layer between the NONIBTDT layer and the top Al electrode. The buffer layer can decrease the possible interface barrier and can totally avoid the contact between the organic layers and the electrodes. The current–voltage (*I*–*V*) characteristics of the memory device ITO/NONIBTDT/LiF/Al are measured under the same condition, as shown in Figure S12 (Supporting Information). The memory device also shows a quaternary memory behavior, which can further rule out the formation of Al filaments in the films and confirm the memory behavior being the interior property of NONIBTDT.

It has been reported that the active layer thickness can affect the electrical memory behavior sometimes. Thus, to consider the relationship between the memory behaviors and the film thicknesses, we investigated the memory performance of the memory device ITO/NONIBTDT/Al with different film thicknesses. According to the SEM images, the film thicknesses of the memory devices were determined to be 50, 70, and 110 nm, respectively. The memory behaviors of the ITO/NONIBTDT/Al devices with different film thicknesses were measured from 0 to –5 V, and the three memory devices all exhibited the quaternary memory effects, as shown in Figure S8–S10 (Supporting Information). This can be concluded that the memory behaviors are independent of film thickness and belong to the interior property of the molecule NONIBTDT.

As the control sample, the sandwich-structured memory device ITO/DNOBTDT/Al was measure under the same condition and the electronic properties of DNOBTDT-based memory devices were also executed in 20 cells. The memory device was initialized in the low-conductance state (OFF state). When an external voltage from 0 to –5 V was gradually applied on the device, two abrupt increases in current were observed at the voltages of –1.50 and –2.76 V, indicating a transition from the low-conductance state ("OFF" state) to the intermediate-conductance state ("ON1") and then to the high-conductance state ("ON2" state), as shown in Figure 2b. Hence, the ITO/DNOBTDT/Al device shows typical ternary data-storage behavior. Thus, we successfully fabricated a quaternary memory device with NONIBTDT containing three electron acceptors and a ternary data-storage device with DNOBTDT consisting of two electron-deficient moieties. Additionally, the threshold voltage of the memory device fabricated with NONIBTDT is higher than that of DNOBTDT-based memory device.

2.4. Proposed Mechanism of Memory Behavior

To understand the electronic properties of NONIBTDT and DNOBTDT-based memory devices, cyclic voltammetry (CV) measurements were carried out on the spin-coated films, as shown in Figure S2 (Supporting Information). The highest occupied molecular orbital (HOMO) and lowest unoccupied molecular orbital (LUMO) energy levels can be calculated from the CV diagram using the following equations: $E_{HOMO} = -[E\text{onset OX} + 4.80 - E_{Ferrocene}]$ and $E_{LUMO} = HOMO + E_g$,[40] where E_g is the optical bandgap, which can be estimated from the onset of ultraviolet–visible (UV–vis) absorption spectra, and the detailed results of both films are summarized in **Table 1**. Hole injection energy barrier from ITO into HOMO energy level of NONIBTDT is 0.60 eV, which is smaller than the

Table 1. Optical and electrochemical properties of the films fabricated with NONIBTDT and DNOBTDT.

Molecule	λ_{onset} [nm]	E_g [a)] [eV]	HOMO [b)] [eV]	LUMO [c)] [eV]	Hole injection [eV]	Electron injection [eV]
NONIBTDT	585	2.12	–05.40	–3.28	0.60	1.02
DNOBTDT	613	2.02	–5.23	–3.21	0.53	1.09

[a)] Estimated from the onset of absorption: bandgap = $1240/\lambda_{onset}$; [b)]HOMO = $-[E_{OX}^{onset}+4.80-E_{Ferrocence}]$; [c)]LUMO = HOMO $+E_g$.

electron injection energy barrier between the work function of Al and LUMO energy level (1.02 eV). Therefore, NONIBTDT is a p-type semiconductor material, and the memory behaviors are dominated by hole transporting, as shown in Figure 3a. Similarly, DNOBTDT is also a p-type material.

HOMO and LUMO energy levels were also calculated through DFT with the B3LYP/6–31G basis set to understand the field-induced CT processes. In order to simplify the simulation, the alkyl chains probably do not affect the memory behaviors and are replaced with methyl groups (Figure 3b). As shown in Figure 3c, the HOMO is almost located on thiophene and carbazole while the LUMOs contribute mainly to the BTD, NA, and NO moieties, which are consistent with the fact that thiophene and carbazole are well-known electron donors, while BTD, NA, and NO moieties are various electron acceptors. Thus, CT process can occur through the conjugated backbones driven by an external electric field. At a low-voltage bias, the molecule is at ground state with a large HOMO–LUMO gap and the device is in the low-conductance state. With the increase in the voltage reaching to the first threshold bias, the charges will transfer from the electron donors (HOMO) to BTD acceptors (LUMO), and the positive and negative charges will be segregated to form a stable CT complex. Consequently, a conductive channel is formed for the transporting of the charges, leading to the ON1 state. The switching voltage from the OFF to the ON1 state matches the HOMO–LUMO energy bandgap in CV measurement. Subsequently, with the increase in the bias up to the second threshold voltage, another CT state will be formed with the charges transferring to the NI moieties at high energy level (LUMO+1), resulting in the formation of the higher conductive (ON2) state. Finally, the third transfer process will generate from HOMO to the NO groups (LUMO+2) under high electric field. This will be responsible for switching from the ON2 state to the ON3 state. Additionally, the dipole moment is measured to be 11.13 D, which indicates that the finally formed complex might be very stable. Therefore, the device can remain in the ON3 state for a long time, leading to the non-volatile memory behavior of molecule NONIBTDT-based memory device. The switching mechanism of DNOBTDT-based memory device is similar to that of NONIBTDT (see the orbital details in Figure S3 in the Supporting Information), despite only two electron acceptors, thus ternary memory behaviors were detected.

In order to verify the CT process in the films, the UV–vis absorption spectra were measured for NONIBTDT-based film on ITO substrates with and without an external electric field, as shown in Figure S11a (Supporting Information). Upon finishing the UV measurement of the film without voltage sweeping, a liquid Hg droplet was deposited on the film serving as the top electrode to measure the electronic properties. Subsequently, Hg was removed after an electrical sweep from 0 to –5 V on the device ITO/NONIBTDT/Hg, and the UV absorption spectrum of the formed film was measured under the same condition. Compared with the UV–vis absorption spectrum in the OFF state, the intensity of that in the ON3 state was increased, indicating the increased concentration of the CT states induced by an external electric field. To further confirm that the CT complex is formed under the condition of an external electric field, fluorescence emission spectra of the film were measured as depicted in Figure S11b (Supporting Information). As we can see, the intensity of the photoluminescence spectrum was quenched significantly in the ON3 state, illustrating that the CT complex was formed under an external voltage.[41] Therefore, the CT process can be confirmed under an electric field and the CT can be applied as the conductive mechanism.

2.5. Thin Film Nanostructure

Besides rational design to achieve different multilevel memory behaviors, molecular stacking in solid state is an effective factor to influence the memory working parameters such as threshold voltages. Thus, measurements in terms of molecular stacking were carried out to understand the larger threshold switching voltage of NONIBTDT-based quaternary storage devices. **Figure 4**a shows the UV–vis absorption spectra of NONIBTDT in CH_2Cl_2 solution and in film state. The maximum absorption peak located at 327 nm attributed to the π–π^* electronic transitions of BTD core. Additionally, the absorption peak between 425 and 576 nm was consistent with the intramolecular and/or intermolecular charge transfer from the electron donors to the electron acceptors. Meanwhile, compared with the absorption peak in solution state, the absorption peak in film state was bathochromic-shifted significantly from 485 to 505 nm. Similarly, the UV absorption spectrum of the DNOBTDT film also undergoes a larger redshift of about 29 nm compared to that in solution state (Figure 4b). These shifts indicate molecular integration and/or ordered stacking of both films.[42] In addition, atomic force microscopy images of surface morphology in Figure S4 (Supporting Information) show that both films present a uniform granular structure. Additionally, the surface root-mean-square roughness was estimated to be 1.575 nm for the NONIBTDT film and 1.682 nm for the DNOBTDT film, which indicates a smooth interface that ensures favorable and stable interfacial contact with electrodes. This smooth surface could effectively prevent Al nanoparticles from diffusion into films during the Al electrode deposition process.[43] Meantime, the smooth surface is beneficial for the decrease of the energy barriers between the active layers and the electrodes.

However, X-ray diffraction (XRD) and grazing incidence small angle X-ray scattering (GISAXS) patterns reveal that DNOBTDT has better molecular stacking than NONIBTDT in the film. For NONIBTDT, the diffraction peaks located at 21.0° corresponding to a *d*-spacing of 4.23 Å indicated a relative ordered arrangement in the films (Figure 4c). Furthermore, the diffraction peaks located at 7.50° and 8.60° represent long-range

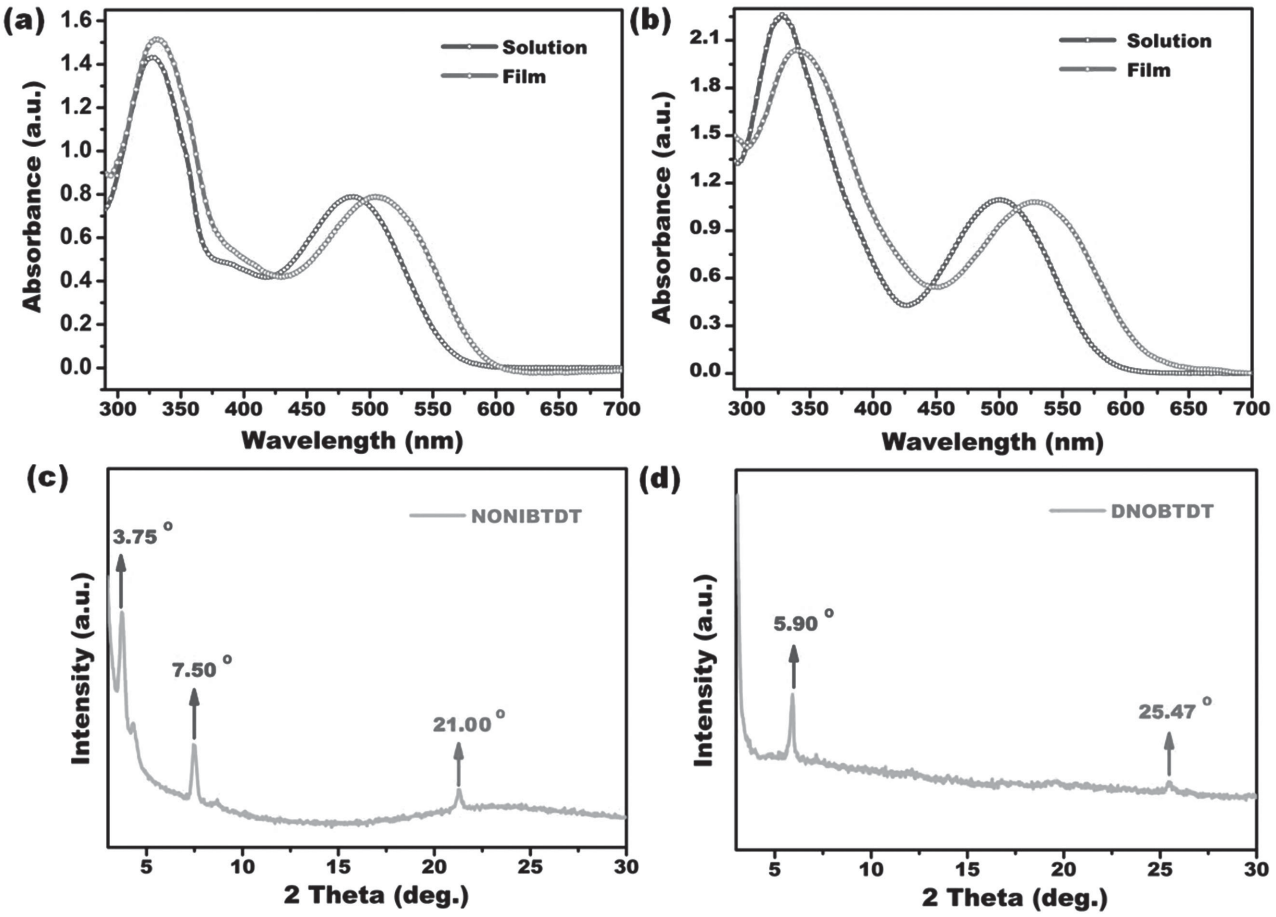

Figure 4. a) UV–vis absorption spectra of NONIBTDT in the CH_2Cl_2 solution and in the thin-film state; b) UV–vis absorption spectra of DNOBTDT in the CH_2Cl_2 solution and in the thin-film state; c) XRD pattern of the spin-coated NONIBTDT films; d) XRD pattern of the spin-coated DNOBTDT films.

ordered arrangements with *d*-spacings of 11.78 and 10.27 Å, respectively. Additionally, the second-order diffraction peaks of 11.78 and 10.27 Å even appear at 3.75° and 4.30°, suggesting the ordered stacking exists in multiple directions. However, the diffraction intensity of the peak located at 7.50° was much stronger and sharper than that located at 8.60°, indicating the orientation was packed almost in the way of 11.78 Å in film state. In the case of DNOBTDT-based films, the diffraction peak located at 25.49° corresponded to a *d*-spacing of 3.49 Å, which was a typical intermolecular π–π interaction distance, and this distance is much smaller than that of our quaternary molecule NONIBTDT (Figure 4d). The left diffraction peak observed at 5.90° with a *d*-spacing of 14.97 Å belonged to a long-range arrangement along a uniform crystal axis. We also calculate the crystalline thickness of the two molecules according to the Scherrer formula and find that the crystalline thickness of molecule DNOBTDT was up to almost 46 nm, which is larger than that of the quaternary molecule NONIBTDT with 28 nm. This also illustrates that the crystalline property of the symmetrical molecule DNOBTDT is better than that of the asymmetrical molecule NONIBTDT with the quaternary memory property. The above stacking discrepancies should be ascribed to the symmetry of the two molecules. DNOBTDT is consisting of two carbazole moieties that processed a large coplanar structure, and the dihedral angle between the carbazole and the thiophene moiety is about 23° (Figure S6, Supporting Information). Its symmetric structure improves the efficiency of stacking. In contrast, NONIBTDT is of a thiophene and a carbazole unit that increased molecular planarity but the two ends of the backbone are composed of different electron acceptors. This asymmetric geometry will deteriorate the packing efficiency of molecules, including closing π–π and long-ranged stacking. Additionally, the dihedral angle between the carbazole and the thiophene moiety is estimated to be 61° and that between the thiophene and the NI moiety is ≈69° for the asymmetric molecule NONIBTDT, which can also explain the larger π–π interaction distance and the weak crystallinity in film state. However, molecule NONIBTDT formed an ordered microstructure in the thin film on the whole. When an external voltage is applied on the device, charge carriers from the ITO electrode will inject into the organic films and can lead to intermolecular/intramolecular charge transfer. Due to the ordered microstructure and smooth surface, the charge carriers can move through the molecular backbone/adjacent molecules easily. Thus, with the increase in the applied voltage, the charges will transfer gradually from the electron donors to the electron acceptors with different energy levels to form various conduction channels and thus three conductive ON states.[44]

In addition, we also carried out the GISAXS measurements to determine the crystalline properties of the two molecule-based films relative to the substrate. **Figure 5**a shows the schematic illustration of GISAXS with a very small incident angle in point collimation mode. As depicted in Figure 5b, the NONIBTDT film shows four circled bands, which are consistent with the four diffraction peaks below 10° in the XRD. The arc-shaped scattering signal indicates the molecular grain is in random orientations with respect to the substrate. Meanwhile, the GISAXS result for DNOBTDT-based film confirms that all molecular grains are of uniform orientation, with a face-on configuration toward the ITO substrate. Such a uniform face-on stacking of crystalline is beneficial to the charge transport and leading to lower power consumption.[34] We also calculate the structural optimizations of these two molecules and find both molecules, NONIBTDT and DNOBTDT, with a height of 15 Å (Figure S6, Supporting Information). Additionally, the long-range stacking distances of NONIBTDT and DNOBTDT were calculated to be 11.78 and 14.97 Å, respectively. Thus, we can conclude that molecule DNOBTDT stands upright on the ITO and each crystal contains about 30 layers of molecule DNOBTDT, while molecule NONIBTDT reclines on the ITO substrate and each crystal consists of about 23 layers of molecule NONIBTDT, as shown in Figure 5b,c. Thus, according to the above analysis, we can draw the conclusion that symmetry can greatly influence the molecular stacking and the crystallinity, which will affect the transporting of the charges in the films, thus the threshold voltage of memory devices. With intensive research in advanced synthesis and material science, we believe that the little defect will be perfectly solved in our following work.

3. Conclusion

In conclusion, we rationally designed a molecule, NONIBTDT, with three electron acceptors and two well-known hole-transporting electron donors in the backbone. Organic quaternary memory behavior is achieved for the first time. Theoretical calculations confirmed the presence of three various electron-deficient moieties through electronic static potential plotting. The switching mechanism of this memory device is contributed to the three charge-transfer processes under an external electric

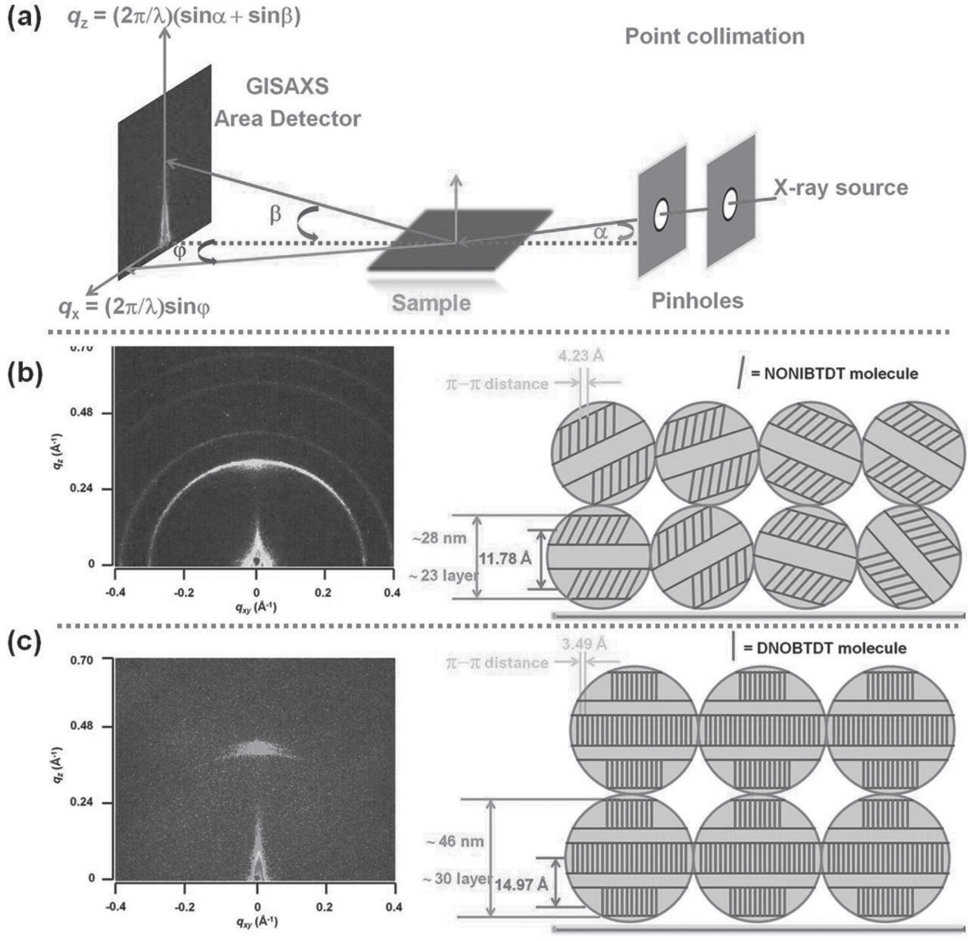

Figure 5. a) Schematic illustration of GISAXS with a 2D image plate applying an incident beam with a glancing angle of $\alpha = 0.20°$. b) GISAXS pattern and the illustration of the NONIBTDT film on ITO substrate. c) GISAXS pattern and the illustration of the DNOBTDT film on ITO substrate. NONIBTDT-based film shows four circled bands in the diffraction graph, indicating that the molecular grains are in random orientations with respect to the substrate. The DNOBTDT-based film shows a single diffraction signal that indicates all molecular grains are of uniform orientation, with a face-on configuration toward the ITO substrate.

field. The higher threshold voltages of NONIBTDT-based quaternary devices than that of DNOBTDT is correlated to the fact that the asymmetric NONIBTDT molecules have less ordered stacking and worse crystallinity in the film devices. This suggests the importance of molecular symmetry in the design of organic multilevel materials, which was traded off in our present work but will be considered in our future work. Our results will be useful to the development of organic multilevel memory device and high-density data-storage devices.

4. Experimental Section

Fabrication of memory devices: The ITO glass was pre-cleaned with water, acetone, and alcohol in an ultrasonic bath for 30 min, respectively. The solution of 10 mg small molecule in 1 mL *o*-dichlorobenzene was filtered through a microfilter equipped with a 0.22 μm sized pinhole. The solution was evaporated under high vacuum (10^{-3} Torr), and the film thickness was decided by the speed of the spin-coating machine. An aluminum layer was thermally evaporated and deposited onto the active film at about 10^{-6} Torr through a shadow mask to form the top electrode. The sandwich-structured memory device area of about 0.0314 mm^2 was obtained. All electrical measurements of the device were taken at ambient conditions, applying an HP 4145B semiconductor parameter analyzer equipped with an HP 8110A pulse generator.

Supporting Information

Supporting Information is available from the Wiley Online Library or from the author.

Acknowledgements

This work was financially supported by the NSF of China (Grant Nos. 21176164, 21206102, 21336005, and 21476152), the NSF of Jiangsu Province (BE2013052), a project supported by the Specialized Research Fund for the Doctoral Program of Higher Education of China (Grant No. 20123201120005), Chinese–Singapore Joint Project (2012DFG41900), and National Excellent Doctoral Dissertation funds (201455). The authors sincerely thank Prof. Peng Wu for beneficial discussion and revision of this work.

Received: August 18, 2015
Revised: September 22, 2015
Published online: November 19, 2015

[1] L. J. Guo, E. Leobandung, S. Y. Chou, *Science* **1997**, *275*, 649.
[2] T. Osaka, M. Takai, K. Hayashi, K. Ohashi, M. Saito, K. Yamada, *Nature* **1998**, *392*, 796.
[3] G. Y. Jiang, T. Michinobu, W. F. Yuan, M. Teng, Y. Q. Wen, S. X. Du, H. J. Gao, L. Jiang, Y. L. Song, F. Diederich, D. B. Zhu, *Adv. Mater.* **2005**, *17*, 2170.
[4] M. H. R. Lankhorst, B. W. S. M. M. Ketelaars, R. A. M. Wolters, *Nat. Mater.* **2005**, *4*, 347.
[5] B. L. Hu, C. Y. Wang, J. X. Wang, J. K. Gao, K. Wang, J. S. Wu, G. D. Zhang, W. Q. Cheng, B. Venkateswarlu, M. F. Wang, P. S. Lee, Q. C. Zhang, *Chem. Sci.* **2014**, *5*, 3404.
[6] S. H. Lee, Y. Jung, R. Agarwal, *Nat. Nanotechnol.* **2007**, *2*, 626.
[7] B. H. Lee, M. K. Ryu, S. Y. Choi, K. H. Lee, S. Im, M. M. Sung, *J. Am. Chem. Soc.* **2007**, *129*, 16034.
[8] T. Rueckes, K. Kim, E. Joselevich, G. Y. Tseng, C. L. Cheung, C. M. Lieber, *Science* **2000**, *289*, 94.
[9] R. Waser, M. Aono, *Nat. Mater.* **2007**, *6*, 833.
[10] N. Xu, L. F. Liu, X. Sun, X. Y. Liu, D. D. Han, Y. Wang, R. Q. Han, J. F. Kang, B. Yu, *Appl. Phys. Lett.* **2008**, *92*, 232112.
[11] C. L. Liu, W. C. Chen, *Polym. Chem.* **2011**, *2*, 2169.
[12] S. Song, B. Cho, T. W. Kim, Y. Ji, M. Jo, G. Wang, M. Choe, Y. H. Kahng, H. Hwang, T. Lee, *Adv. Mater.* **2010**, *22*, 5048.
[13] J. G. Park, W. S. Nam, S. H. Seo, Y. G. Kim, Y. H. Oh, G. S. Lee, U. G. Paik, *Nano. Lett.* **2009**, *9*, 1713.
[14] a) Y. Jung, S. H. Lee, A. T. Jennings, R. Agarwal, *Nano. Lett.* **2008**, *8*, 2056; b) C. Y. Wang, P. Y. Gu, B. L. Hu, Q. C. Zhang, *J. Mater. Chem. C* **2015**, *3*, 10055.
[15] Y. Hou, Y. W. Cheng, T. Hobson, J. Liu, *Nano. Lett.* **2010**, *10*, 2727.
[16] a) S. F. Miao, H. Li, Q. F. Xu, Y. Y. Li, S. J. Ji, N. J. Li, L. H. Wang, J. W. Zheng, J. M. Lu, *Adv. Mater.* **2012**, *24*, 6210; b) S. F. Miao, H. Li, Q. F. Xu, N. J. Li, J. W. Zheng, R. Sun, J. M. Lu, C. M. Li, *J. Mater. Chem.* **2012**, *22*, 16582; c) S. F. Miao, Y. X. Zhu, H. Zhuang, X. P. Xu, H. Li, R. Sun, N. J. Li, S. J. Ji, J. M. Lu, *J. Mater. Chem. C* **2013**, *1*, 2320.
[17] a) H. Zhuang, Q. J. Zhang, Y. X. Zhu, X. F. Xu, H. F. Liu, N. J. Li, Q. F. Xu, H. Li, J. M. Lu, L. H. Wang, *J. Mater. Chem. C* **2013**, *1*, 3816; b) H. Zhuang, Q. H. Zhou, Y. Li, Q. J. Zhang, H. Li, Q. F. Xu, N. J. Li, J. M. Lu, L. H. Wang, *ACS. Appl. Mater. Inter.* **2014**, *6*, 94; c) X. M. Wang, D. Wang, G. Y. Zhou, W. Yu, Y. T. Zhou, Q. F. Fang, M. H. Jiang, *J. Mater. Chem* **2001**, *11*, 1600.
[18] a) P. Y. Gu, F. Zhou, J. K. Gao, G. Li, C. Y. Wang, Q. F. Xu, Q. C. Zhang, J. M. Lu, *J. Am. Chem. Soc.* **2013**, *135*, 14086; b) P. Y. Gu, J. Gao, C. J. Lu, W. Chen, C. Wang, G. Li, F. Zhou, Q. F. Xu, J. M. Lu, Q. Zhang, *Mater. Horizons.* **2014**, *1*, 446; c) C. Y. Wang, J. X. Wang, P. Z. Li, J. K. Gao, S. Y. Tan, W. W. Xiong, B. L. Hu, P. S. Lee, Y. L. Zhao, Q. C. Zhang, *Chem Asian J.* **2014**, *9*, 779; d) D. M. DeLongchamp, R. J. Kline, D. A. Fischer, L. J. Richter, M. F. Toney, *Adv. Mater.* **2011**, *23*, 319.
[19] a) C. T. Poon, D. Wu, W. H. Lam, V. W. W. Yam, *Angew. Chem. Int. Ed. Engl.* **2015**, *54*, 1; b) G. Li, K. Zheng, C. Y. Wang, K. S. Leck, F. Z. Hu, X. W. Sun, Q. C. Zhang, *ACS Appl. Mater. Inter.* **2013**, *5*, 6458; c) J. B. Li, Q. C. Zhang, *ACS Appl. Mater. Inter.* **2015**, DOI: 10.1021/acsami.5b00113.
[20] M. Emmelius, G. Pawlowski, H. W. Vollmann, *Angew. Chem. Int. Ed. Engl.* **1989**, *28*, 1445.
[21] S. Kawata, Y. Kawata, *Chem. Rev.* **2000**, *100*, 1777.
[22] M. Alexe, C. Harnagea, A. Visinoiu, A. Pignolet, D. Hesse, U. Gosele, *Scr Mater.* **2001**, *44*, 1175.
[23] H. Li, Q. F. Xu, N. J. Li, R. Sun, J. F. Ge, J. M. Lu, H. W. Gu, F. Yan, *J. Am. Chem. Soc.* **2010**, *132*, 5542.
[24] S. J. Liu, P. Wang, Q. Zhao, H. Y. Yang, J. Wong, H. B. Sun, X. C. Dong, W. P. Lin, W. Huang, *Adv. Mater.* **2012**, *24*, 2901.
[25] M. J. Lee, C. B. Lee, D. Lee, S. R. Lee, M. Chang, J. H. Hur, Y. B. Kim, C. J. Kim, D. H. Seo, S. Seo, U. I. Chung, I. K. Yoo, K. Kim, *Nat. Mater.* **2011**, *10*, 625.
[26] R. Waser, R. Dittmann, G. Staikov, K. Szot, *Adv. Mater.* **2009**, *21*, 2632.
[27] T. Chattopadhyay, J. N. Roy, A. K. Chakraborty, *Opt. Commun.* **2009**, *282*, 1287.
[28] S. Lee, D. Y. Shin, S. J. Chung, X. Liu, J. K. Furdyna, *Appl. Phys. Lett.* **2007**, *90*, 152113.
[29] B. F. Soares, F. Jonsson, N. I. Zheludev, *Phys. Rev. Lett.* **2007**, *98*, 153905.
[30] T. Yoo, S. Khym, S. Y. Yea, S. Chung, S. Lee, X. Liu, J. K. Furdyna, *Appl. Phys. Lett.* **2009**, *95*, 202505.
[31] R. Zarnetta, R. Takahashi, M. L. Young, A. Savan, Y. Furuya, S. Thienhaus, B. Maass, M. Rahim, J. Frenzel, H. Brunken,

Y. S. Chu, V. Srivastava, R. D. James, I. Takeuchi, G. Eggeler, A. Ludwig, *Adv. Funct. Mater.* **2010**, *20*, 1917.
[32] M. Wang, X. W. Hu, P. Liu, W. Li, X. Gong, F. Huang, Y. Cao, *J. Am. Chem. Soc.* **2011**, *133*, 9638.
[33] a) L. Burgi, M. Turbiez, R. Pfeiffer, F. Bienewald, H. J. Kirner, C. Winnewisser, *Adv. Mater.* **2008**, *20*, 2217; b) P. P. Khlyabich, B. Burkhart, C. F. Ng, B. C. Thompson, *Macromolecules* **2011**, *44*, 5079.
[34] a) Y. Li, H. Li, H. F. Chen, Y. Wan, N. J. Li, Q. F. Xu, J. H. He, D. Y. Chen, L. H. Wang, J. M. Lu, *Adv. Funct. Mater.* **2015**, *25*, 4246; b) G. Wang, S. F. Miao, Q. J. Zhang, H. F. Liu, H. Li, N. J. Li, Q. F. Xu, J. M. Lu, L. H. Wang, *Chem. Commun.* **2013**, *49*, 9470.
[35] a) H. F. Liu, H. Zhuang, H. Li, J. M. Lu, L. H. Wang, *Phys. Chem. Chem. Phys.* **2014**, *16*, 17125; b) W. S. Ren, H. Zhuang, Q. Bao, S. F. Miao, H. Li, J. M. Lu, L. Wang, *Dyes Pigm.* **2014**, *100*, 127.
[36] B. K. Kuila, S. Malik, S. K. Batabyal, A. K. Nandi, *Macromolecules* **2007**, *40*, 278.
[37] P. Sonar, S. P. Singh, P. Leclere, M. Surin, R. Lazzaroni, T. T. Lin, A. Dodabalapur, A. Sellinger, *J. Mater. Chem.* **2009**, *19*, 3228.
[38] L. Biniek, S. Fall, C. L. Chochos, N. Leclerc, P. Leveque, T. Heiser, *Org. Electron* **2012**, *13*, 114.
[39] H. L. Pan, Y. N. Li, Y. L. Wu, P. Liu, B. S. Ong, S. P. Zhu, G. Xu, *J. Am. Chem. Soc.* **2007**, *129*, 4112.
[40] C. Y. Wang, J. Zhang, G. K. Long, N. Aratani, H. Yamada, Y. Zhao, Q. C. Zhang, *Angew. Chem. Int. Ed. Engl.* **2015**, *54*, 6292.
[41] Y. L. Liu, K. L. Wang, G. S. Huang, C. X. Zhu, E. S. Tok, K. G. Neoh, E. T. Kang, *Chem. Mater.* **2009**, *21*, 3391.
[42] R. Schmidt, J. H. Oh, Y. S. Sun, M. Deppisch, A. M. Krause, K. Radacki, H. Braunschweig, M. Konemann, P. Erk, Z. A. Bao, F. Wurthner, *J. Am. Chem. Soc.* **2009**, *131*, 6215.
[43] X. D. Zhuang, Y. Chen, G. Liu, B. Zhang, K. G. Neoh, E. T. Kang, C. X. Zhu, Y. X. Li, L. J. Niu, *Adv. Funct. Mater.* **2010**, *20*, 2916.
[44] P. Y. Gu, Y. Ma, J. H. He, G. K. Long, C. Y. Wang, W. Q. Chen, Y. Liu, Q. F. Xu, J. M. Lu, Q. C. Zhang, *J. Mater. Chem. C* **2015**, *3*, 3167.